Monthly Notices of the ROYAL ASTRONOMICAL SOCIETY

MNRAS **549,** 1–14 (2026)
Advance Access publication 2026 May 23

https://doi.org/10.1093/mnras/stag955

[O III] line ratios and evolution of oxygen abundance with redshift using *JWST*–VLT–Keck observations

Vidit Bhandari,[1] Mingyi Xu,[2] Sultana N. Nahar[2] and Anil K. Pradhan[2,3]★

[1]*Department of Physics, Denison University, Granville, OH, USA*
[2]*Department of Astronomy, The Ohio State University, Columbus, OH 43210, USA*
[3]*Department of Chemistry, Chemical Physics Program, The Ohio State University, Columbus, OH 43210, USA*

Accepted 2026 May 15. Received 2026 May 4; in original form 2026 February 10

ABSTRACT

We study high-z galaxies using *James Webb Space Telescope* observations and new atomic data, complemented by low-z observations from VLT and Keck, to examine a sample of 44 galaxies and analyse or re-analyse observed [O III] line ratios to derive electron temperatures, densities, and oxygen abundances. In addition to [O III] temperature diagnostics, [O II] and [S II] ratios are employed for density constraints and contour plots of physical conditions. Based on nebular temperature-abundance relations for H II regions, we track the evolution of [12 + log(O/H)] with redshift. Our [O III] atomic model incorporates recombination-cascade contributions to forbidden lines using new level-specific recombination rate coefficients and transition probabilities, together with collision strengths computed in earlier works. We find that individual galaxies show a large and systematic variation with electron temperature in the nebular range 5000–25 000K, and O-abundance down to 6.75 compared to the solar value 8.70. The oxygen abundances versus z display a broadly decreasing trend towards high-$z \sim 10$, with a best fit ranging from 8.25 to 7.50 from the present epoch at $z = 0$, generally consistent with previous works on metallicity-redshift variation. The present analysis employs a collisional-radiative-recombination model that also considers possible (e + O IV) –> O III recombination-cascade contributions to [O III] forbidden lines, but is found to be negligible. We also explore AI Machine Learning models to predict and complement directly derived results, with preliminary simulations trained on observed flux ratios and PyNeb-simulated data sets that are promising but limited by current sample sizes. Future work may expand these data sets and further refine statistical models.

Key words: galaxies: abundances – galaxies: high-redshift – H II regions – line: formation – atomic data – atomic processes.

1 INTRODUCTION

Understanding chemical evolution of galaxies has been dramatically revised by the *James Webb Space Telescope* (*JWST*) observations up to high redshifts $z \sim 14$, which reveal metal-rich systems forming within a few hundred million years after the big bang. Space-based observations of distant high-z galaxies by *JWST* have definitively established that galaxy formation began much earlier than believed hitherto (e.g. K. Z. Arellano-Córdova et al. 2022a; R. L. Sanders et al. 2023a, Glass-*JWST* Early Release Science Program. IV; S. Mascia et al. 2024). That became evident from a number of clearly resolved atomic lines from several elements other than H and He. Furthermore, since the observed spectra are in the near-IR range the observations can also be verified and complemented by ground-based observations, particularly by high-resolution spectrographs at large telescopes such as Keck and Very Large Telescope (VLT). Thus optical or even near-UV lines are observable from red-shifted objects. Since *JWST* spectra became available, it was noticed that several well-known lines of oxygen ions were prominent in the spectra of galaxies out to z $\sim$ 10 or greater. As oxygen is one of the most common elements, its abundance would therefore be a reliable indicator of the chemical evolution of the universe if determined accurately and from a sufficient number of galaxies. In particular, the forbidden [O III] emission lines prominently stands out in many of these *JWST* obsai-astrophysiocat26.pdfervations and have been used to study local physical conditions and correlations among supernovae (SNe) rates, stellar formation, galactic outflows, and galaxy masses. For example, a mass–metallicity relation has been inferred, and which shows metallicity ranges significantly smaller than the present Milky Way or solar values. Also, large equivalent widths of [O III] lines have been observed, implying intense radiation fields from massive stars and blue-shifted lines from SNe and galactic outflows. Another recent study of *JWST*/NIRSpec spectra examining the mass–matellacity-redshift correlations finds a significant but not large deviations from a trend towards lower metallicities with increasing redshfits (A. Sarkar et al. 2024).

★ E-mail: pradhan.1@osu.edu

In our sample, we consider the earliest one at $z \sim 10$ (Abdurro'uf et al. 2024; T. Y.-Y. Hsiao et al. 2024, 2025), and the latest at $z \sim 1$, observed with *JWST* (B. Welch et al. 2024). Doubly-ionized oxygen O III is well-known in observations from nebular and active galactic nucleus (AGN) and H II regions. The forbidden [O III] lines have been studied extensively and are used widely as temperature diagnostics in H II regions in the range 1000–20 000 K. In addition, forbidden [O II] and [S II] lines are employed as electron density diagnostics (e.g. A. K. Pradhan & S. N. Nahar 2011; M. A. Dopita & R. S. Sutherland 2013). Together, these ions provide temperature–density information, which, in turn, can be parametrized to derive oxygen abundance since only a few ionization states are involved. Useful expressions depend on temperature and density, and have been utilized to obtain abundances in H II regions (e.g. Izotov *et al.* 2006; Mendez-Delgado *et al.* 2023), expressed as 12 + log(O/H) for O relative to H. A recent work has applied strong line calibration on deriving 12 + log(O/H) vz. z relation out to $z\sim$ 3.3 using data from earlier instruments such as Keck for certain masses of galaxies (S. Jain et al. 2025). The *JWST* data with considering the theoretical atomic models is more accurateai-astrophys-iocat26.pdf to consider high-redshift galaxies out to $z\sim$ 10. The primary requirement in order to employ theoretical models to analyse observations is accurate atomic data for relevant physical processes. In the case of forbidden lines, which usually arise from transitions among low-lying energy levels of the same electronic configuration and parity, those data primarily entail electron impact excitation (EIE) and radiative transition probabilities. The dominant transitions are among levels of the ground configuration of the same parity via magnetic dipole (M1) and electric quadruple (E2) transitions. High-precision atomic data have been computed for all ions under study in this work: O II, O III, and S II (references in A. K. Pradhan & S. N. Nahar 2011, and in this work). We employ these data in a spectral modelling code SPECTRA that constructs a radiative-collisional atomic model with a five-level energy structure to obtain line emissivities and ratios. A new extension of SPECTRA is to eai-astrophys-iocat26.pdfxtend the atomic model to include level-specific (e + ion) recombination coefficients from accurate R-matrix calculations from the data base NORAD (S. Nahar 2020; K. Hoy, S. N. Nahar & A. K. Pradhan 2023). The extended collisional-radiative-recombination (CRR) model incorporates (e + ion) rai-astrophys-iocat26.pdfecombination to a number of excited levels, and radiative decays therefrom, into the upper levels that give rise to the observed forbidden lines.

Finally, we compare with previous works to place the results obtained in the context of the mass–metallicity relation and the fundamental metallicity relation for chemical evolution of galaxies, with particular reference to oxygen and iron abundances (e.g. C. A. Tremonti et al. 2004; F. Mannucci et al. 2010).

2 OBSERVATIONAL DATA ANALYSIS

Spectral data for 30 galaxies observed with *JWST*/NIRSpec, ground-based observations of five galaxies from Keck/KCWI/NIRSPEC/MOSFIRE, 7 galaxies from VLT/Shooter, 1 galaxy from CLASSY, and 1 galaxy from MOSDEF was analysed (see references). In addition, data from a few other ground-based instruments was also obtained from literature. Detailed information on data sources is given in Tables A1 and A2 (see the Appendix, along with reported quantitative fluxes for [O III], [O II], and [S II] lines, as well as H β fluxes.

The *JWST* line data in our collection are all from $z > 1$. For analysing some galaxies for approximate comparison in the low-z region, we added a few galaxies from ground-based observations. The data used for lower redshift ground-based observations does not include all ground-based observations until the present epoch but a representative sample of a fewai-astrophys-iocat26.pdf points. For the galaxies that appears twice in the tables, they are analysed using different sets of line fluxes data, as shown in Table A1. The results are arranged in the same order when reproduced in Table A3.

We collected the data for galaxies whose observed fluxes have been reported for determining spectral properties, namely unblended [O II] λλ 3729, 3726 or unblended [S II] λλ 6717, 6732 FS doublet formed by atomic structure and transitions $^4S^o_{3/2} - ^2D^o_{3/3,5/3}$ that are standard density diagnostics, the temperature diagnostic [O III] λλ 4363, 5007 lines due to the atomic transitions $^1D_2 - ^1S_0$ and $^3P^o_2 - ^1D_2$, respectively, that have been identified and extracted until recently available observations.

There are several cases where there are some lines missing from papers in literature. However, our line ratios analysis attempts to estimate their intensities from theoretical line emissivity calculations described below. In particular, if [O III] λ 4959 is missing (necessary for the Oxygen abundance formula from Y. I. Izotov et al. 2006), we calculate its intensity since the ratio [O III] λ 5007/ λ 4959 = 2.88 is constant. That is because both transitions originate from the same upper level and the intensity ratio is determined by their respective A-values, and independent of environment temperature or density. In cases where [O II] λλ 3729, 3726 lines are missing then we employ the [O II] λλ 7320, 7332 lines due to forbidden transitions $2s^2p^3(^2D^o_{3/2} - ^2P^o_{1/2,3/2})$ (c.f. Izotov et al. 2006).

3 THEORY AND COMPUTATIONAL METHOD AND ATOMIC DATA

The calculations described in this paper employ high-accuracy atomic data computed using the powerful R-matrix method and subsidiary codes described in this section. The CRR model includes atomic parameters discussed in the following subsections.

3.1 Energy levels and Einstein A coefficients

The energy level data for O III is computed using the R-matrix method (Nahar 1998) but substituted using observed energies where available from the National Institute of Standards and Technology Atomic Spectra Database (https://physics.nist.gov/asd). The transition probabilities and A-coefficients are also obtained from previous R-matrix calculations and archived in the data base Nahar-OSU-Radiative-Atomic-Database (NORAD; S. Nahar 2020).

We consider an atomic model of O III including the 10 well-known forbidden transitions among the five even-parity levels of the ground configuration $1s^22s^22p^2$: $^3P_{0,1,2}, ^1D_2, ^1S_0$. These levels are considered for collisional excitation and radiation decay in a collisional-radiative model to compute line ratios. In addition, and for the extended CRR model including (e + ion) recombination into higher levels and radiative cascades therefrom, excited electronic configurations up to $n = 10$ are included. The CRR model includes 503 fine structure levels in total, with Einstein A coefficients for transitions among them to calculate radiative-cascade matrix from 453 recombination-populated levels. Some levels with same spin multiplicity (2S+1) are indistinguishable

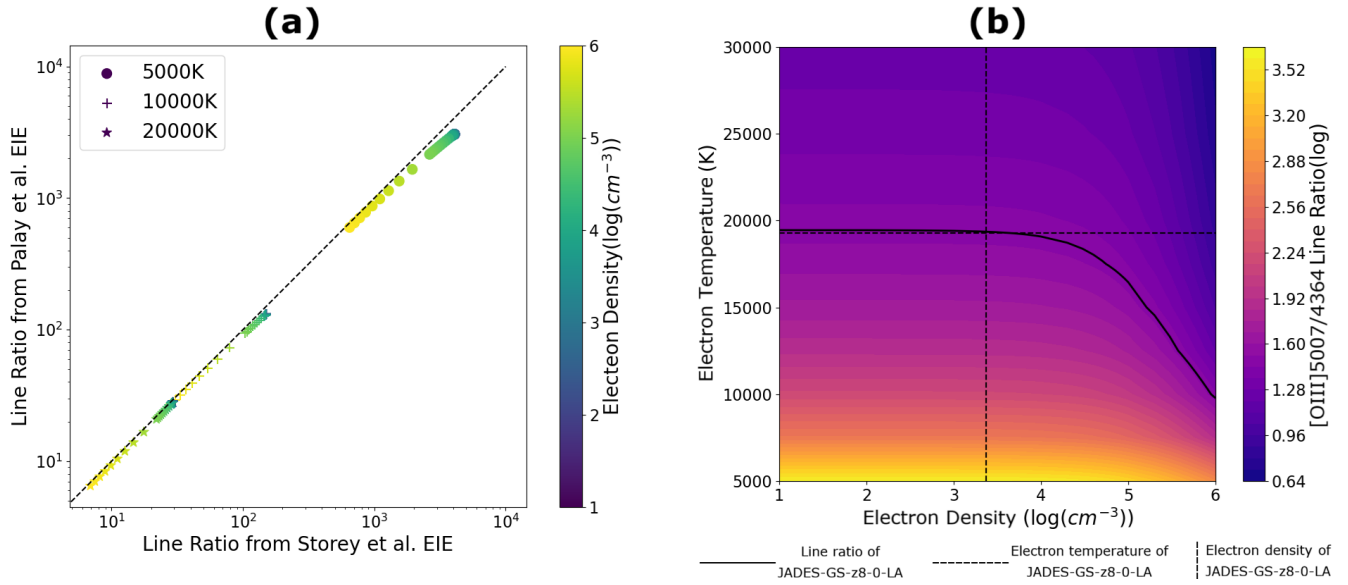

Figure 1. a) Comparison between the [O III] λ 5007/ λ 4363 line ratio results of SPECTRA code by using P. J. Storey & T. Sochi (2015) and E. Palay et al. (2012) effective collisional strength data. Electron temperatures are represented by different marker shapes (circles, pluses, and stars), as indicated in the legend. Electron densities are represented by the colours of the data points, ranging from low (blue) to high (yellow). Each data point corresponds to a pair of line ratios (x and y), computed with the SPECTRA code using two input sources(P. J. Storey & T. Sochi 2015 and E. Palay et al. 2012). (b) [O III] λ 5007/ λ 4363 line ratio contours results of SPECTRA code by using P. J. Storey & T. Sochi (2015) effective collisional strength data. Three lines intersect at a point that determines the position of an example galaxy, JADES-GS-z8-0-LA, in this graph. The vertical line indicates its electron density, the horizontal line indicates its electron temperature, and the thick black curve represents its observed line ratio data (J. Witstok et al. 2024).

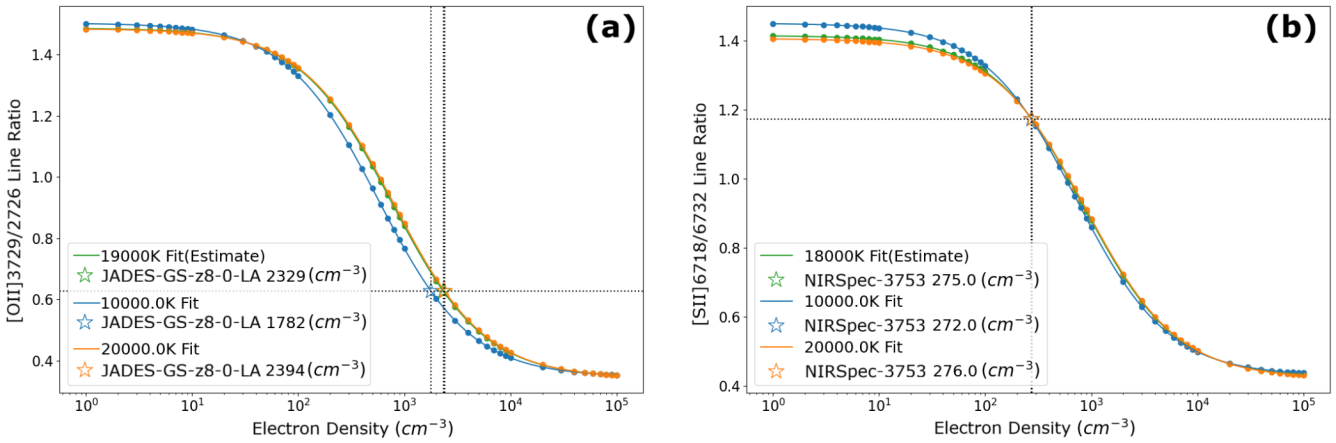

Figure 2. (a) [O II] λ 3729/ λ 3726 density diagnotics. (b) [S II] λ 6718/ λ 6732 density diagnotics.

from multiple orbital angular momentum(L) from the data base NORAD (S. Nahar 2020). We simply use Hund's rule as a guide to assign the lowest energy level among them with the highest L value.

3.2 Electron impact excitation

We consider collision strengths and Maxwellian averaged rate coefficients for the forbidden [O III] ground configuration transitions as in earlier works (E. Palay et al. 2012, P. J. Storey & T. Sochi 2015). The two sets of data agree within a few per cent throughout most of the temperature range of interest in nebulae, but differ somewhat at low electron temperatures $T_e < 1000K$ where the latter are to be preferred. That is because P. J. Storey & T. Sochi (2015) include additional correlation in the wavefunction expansion for the [O III] levels that include the excited configuration $1s^2 2p^6$ that correlates with the quasi-degenerate $^1S_0$ level of the ground configuration $1s^2 2s^2 2p^4$. That additional correlation gives rise to somewhat lower resonance structures near the excitation thresholds up to the $^1S_0$ level, resulting Maxwellian averaged collision strengths that differ from E. Palay et al. (2012). However, as we compare and show in Fig. 1(a), the line emissivity ratios in the range of interest herein is not affected in using the two sets of EIE data which agree without significant differences.

3.3 Electron-ion recombination

In order to discern possible effects due to (e + ion) recombination, i.e. (e + O IV) → O III, we considerably expand the set of excited energy levels of O III. That enables recombination into excited levels followed by radiative cascades to the five levels that give rise to the observed forbidden lines via dipole allowed transitions down to upper levels. The CRR code uses the extensive data sets for level-specific (e + ion) recombination (S. N. Nahar 1999) and A-values from the data base NORAD (S. Nahar 2020) needed to construct the radiative-cascade matrices. Contributions to upper level populations from (e + ion) recombination is then computed by SPECTRA code for particular [O II], [S II], and [O III] lines.

The current state specific recombination rate coefficient (RRC) from the data base NORAD (S. N. Nahar 1999) contains only energy levels from LS coupling, while our atomic modelling is based on fine structure (FS) levels where total angular momentum is identified for level splitting. Based on the statistical weight of each FS level, we split the RRC contribution to each FS level from LS terms as $\mathrm{RRC_{FS}} = \frac{2J+1}{(2L+1)(2S+1)}\mathrm{RRC_{LS}}$. Then, 453 of these 503 levels are used to compute recombination contribution, split from 283 terms by statistical weights, while the other 50 levels that are not available for [O III] RRC data from NORAD are not assigned. However, these 50 levels are included when considering indirect cascades from higher levels with corresponding Einstein A coefficients.

3.4 Line emissivities and ratios

The CRR model is incorporated in a code SPECTRA that computes line emissivities and diagnostic ratios from the data described above. There are two versions of SPECTRA in Fortran and C++ that have been compared against each other (Hoy et al. 2023).

The procedure adopted relies on the canonical [O III] λ 5007/ λ 4363 line ratio that is known to be dependent on electron temperature, and the [O II] λ 3729/ λ 3726 and [S II] λ 6717/ λ 6731 line ratios that are sensitive to electron density. However, as we note below, there are two sets of [O III] theoretical collision strengths available in literature: Palay et al. (2012) and Storey and Sochi (2015). We compute and compare the two sets in Fig. 1(a), and find little difference in the nebular temperature range under consideration (see Section 3.2). Using the later Storey and Sochi (2015) data, and [O II] and [S II] collision strengths, we construct a contour plot of the full electron temperature-density range shown in Fig. 1(b).

The recombination contribution to line ratio result is found to be negligible for [O III] λ 5007/ λ 4363 line ratio within the range of electron temperature and density we consider. To each data point, the contribution is far less than 1 per cent. This difference between including RRC contribution or not including RRC contribution do not make a noticeable difference for line ratio diagnostic of [OIII] λ 5007/ λ 4363.

4 RESULTS

Once the temperature and density are determined from line emissivities and observed line intensity ratios we may derive the oxygen abundance. For oxygen abundance calculations, we adopt two different empirical formulae by Y. I. Izotov et al. (2006) and J. E. Méndez-Delgado et al. (2023), respectively.

4.1 Formula by Y. I. Izotov et al. (2006)

Izotov et al. (2006) re-evaluated empirical expressions for abundance determination from spectral data from emission line galaxies using the Sloan Digital Sky Survey (SDSS) for several elements. The inputs for this formula are relative line fluxes to Hβ, N_e, and T_e. First, it defines $t = 10^{-4}T_e([\mathrm{O\ III}])$ and $x = 10^{-4}N_e t^{-0.5}$. The following formulae are used in this work:

$$12 + \log(\mathrm{O^+/H^+}) = \log\left(\frac{[\mathrm{O\ II}]\ \lambda\ 3727}{\mathrm{H}\beta}\right) + 5.961 + \frac{1.676}{t} - 0.40\log(t) - 0.034t + \log(1 + 1.35x) \quad (1)$$

$$12 + \log(\mathrm{O^+/H^+}) = \log\left(\frac{[\mathrm{O\ II}]\ \lambda\ 7320 + [\mathrm{O\ II}]\ \lambda\ 7330}{\mathrm{H}\beta}\right) + 6.901 + \frac{2.487}{t} - 0.483\log(t) - 0.013t + \log(1 - 3.48x) \quad (2)$$

$$12 + \log(\mathrm{O^{2+}/H^+}) = \log\left(\frac{[\mathrm{O\ III}]\ \lambda\ 4959 + [\mathrm{O\ III}]\ \lambda\ 5007}{\mathrm{H}\beta}\right) + 6.200 + \frac{1.251}{t} - 0.55\log(t) - 0.014t. \quad (3)$$

[O II] λ 3727 represents the total(blended) relative flux of [O II] λ 3726 and [O II] λ 3729 to Hβ. If [O II] λ 3727 is available, we could use (1) to calculate the O II abundance. If [O II] λ 3727 is not available, we could use [O II] λ 7320 + [O II] λ 7330 relative fluxes by (2) to calculate the O II abundance. Also, using (3) with [O III] λ 4959 relative flux, [O III] λ 5007 relative flux, and electron temperature, we can calculate O III abundance. Once we have the abundance for singly ionized state(O II) and doubly ionized state (O III), we can add them up as equation (4) to get the total oxygen abundance:

$$\frac{\mathrm{O}}{\mathrm{H}} = \frac{\mathrm{O^+}}{\mathrm{H^+}} + \frac{\mathrm{O^{2+}}}{\mathrm{H^+}}. \quad (4)$$

For a specific galaxy PJ308-21, the original paper R. Decarli et al. (2024) gives neither [O II] λ 3729+λ 3726 nor [O II] λ 7320+λ 7330 fluxes for using Y. I. Izotov et al. (2006) oxygen abundance formula (1) or (2) to calculate $12 + \log(\mathrm{O^+/H^+})$. We then assume three different values for [O II] λ 3729+λ 3726 relative flux to Hβ: 0.5, 1.0, and 2.0. This assumption is based on the fact that most of other galaxies we examined have [O II] λ 3729+λ 3726 relative flux to Hβ around the range 0.5–2.0. Only the abundance formula (1) from Y. I. Izotov et al. (2006) is used with this assumed [O II] λ 3729+λ 3726 relative flux for PJ308-21, and density determination was done by using [S II] lines. We find that results under such assumption are quite similar, $12 + \log(\mathrm{O/H}) = 7.99$, 8.02, and 8.07, respectively. The another result for PJ308-21, by using another oxygen abundance formula from J. E. Méndez-Delgado et al. (2023) (will be discussed in 4.3), is $12 + \log(\mathrm{O/H}) = 7.95$, which is quite similar to the results by assuming [O II] λ 3729+λ 3726 flux relative to Hβ with using Y. I. Izotov et al. (2006) oxygen abundance formula (1). The first result $12 + \log(\mathrm{O/H}) = 7.99$ is then adopted in the abundance over temperature, redshift, and lookback time plots.

4.2 Formula by J. E. Méndez-Delgado et al. (2023)

Whereas Y. I. Izotov et al. (2006) express the overall oxygen abundance in terms of temperature and density dependence

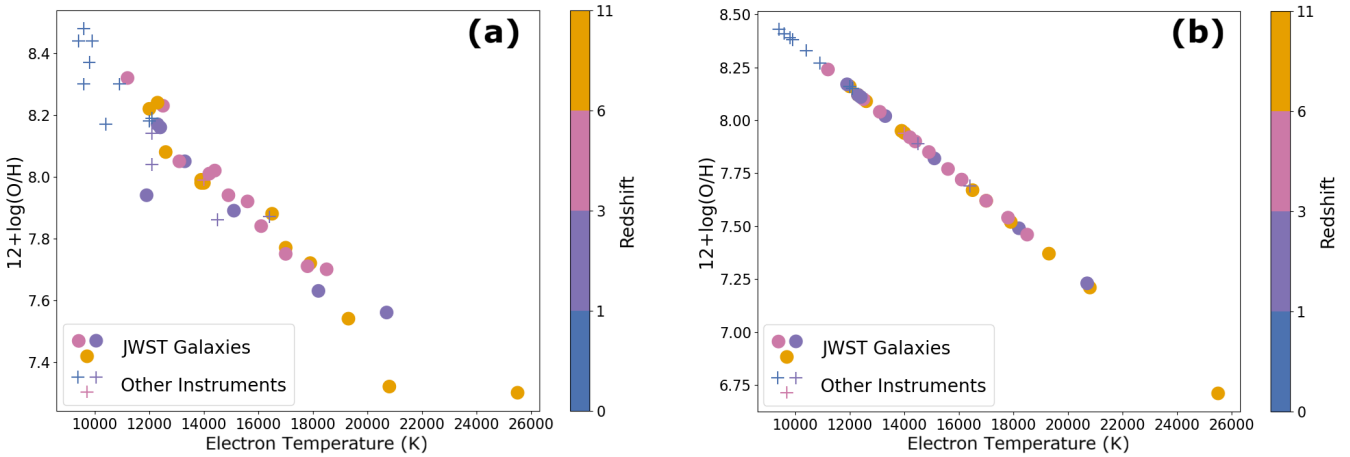

Figure 3. Oxygen abundance evolution with temperature using Y. I. Izotov et al. (2006) formula (a) and J. E. Méndez-Delgado et al. (2023) formula (b).

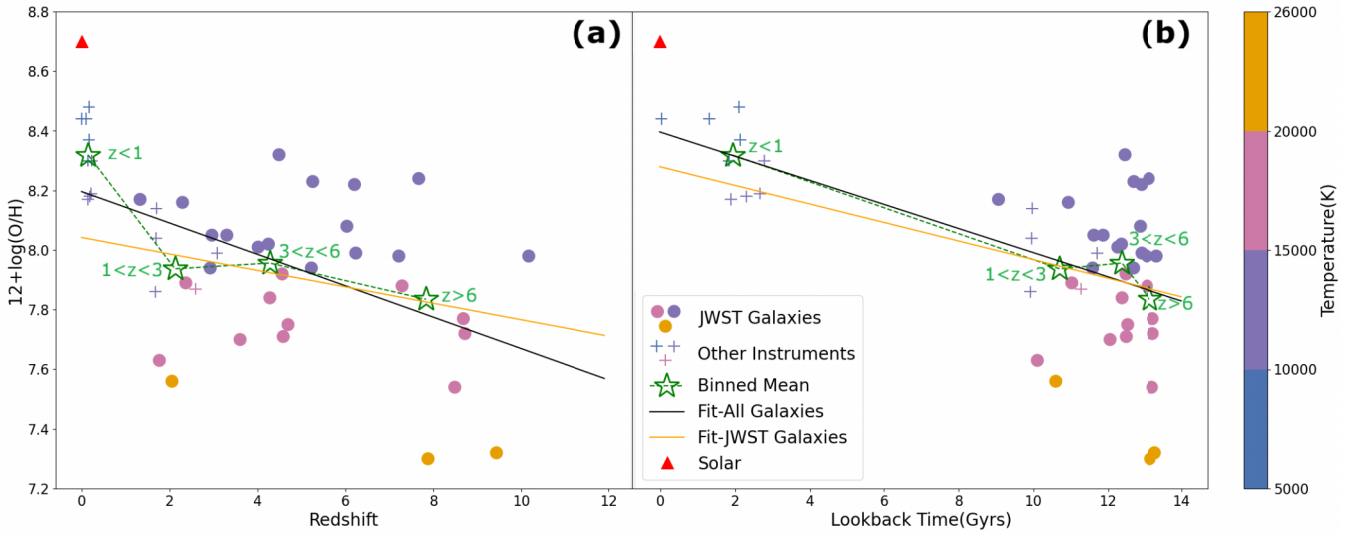

Figure 4. Oxygen abundance evolution with redshift (a) and lookback time (b) using Y. I. Izotov et al. (2006) formula.

of O II and O III (equations 1–3), J. E. Méndez-Delgado et al. (2023) have presented empirical relations for the estimation of temperature and metallicity tacking account of temperature inhomogeneities in H II regions. They estimate temperature fluctuations via a factor t^2 as the deviation from a mean temperature T_0, and derive the following expression for the oxygen abundance:

$$12+\log(\mathrm{O/H})=(-1.07\pm0.09)\times10^{-4}T_0(\mathrm{H}^+)+(9.44\pm0.08), \quad (5)$$

where T_0 is the average temperature of ionized gas, which we take to be $\approx T_e$ (O III) following J. E. Méndez-Delgado et al. (2023). This is justified even if $t^2 > 0$ when one considers temperatures obtained from recombination lines as T_e([N II] λ5755/λ6584) $\approx T_0$ (O II). That is because in the regions of low ionization the emission of H I recombination is essentially from the volume of O II where temperature inhomogeneities are negligible, or $t^2 \approx 0$.

4.3 Oxygen abundance versus redshift and lookback time

Fig.3 presents the results for O-abundance for all galaxies studied herein using both the Y. I. Izotov et al. (2006) and J. E. Méndez-Delgado et al. (2023) empirical formulae given above, plotted against electron temperature and colour coded according to redshift z. Figs 4 and 5 show the results of O/H versus z and lookback time in Gyrs, with temperature shown in the colour coded bar. The lookback time was calculated from redshifts by Astropy Planck18 instance of Flat ΛCDM cosmology. The results in Figs 4 and 5 also show redshift ranges $0 < z < 1$, $1 < z < 3$, $3 < z < 6$, and $6 < z < 11$, superimposed on a linear best-fit through the data.

4.4 Machine learning analysis

To complement the direct abundance derivations, we employ machine learning techniques to identify patterns in the parameter space and quantify predictive relationships. Our analysis uses 45 galaxies with complete measurements of z, T_e[O III], and 12 + log(O/H).

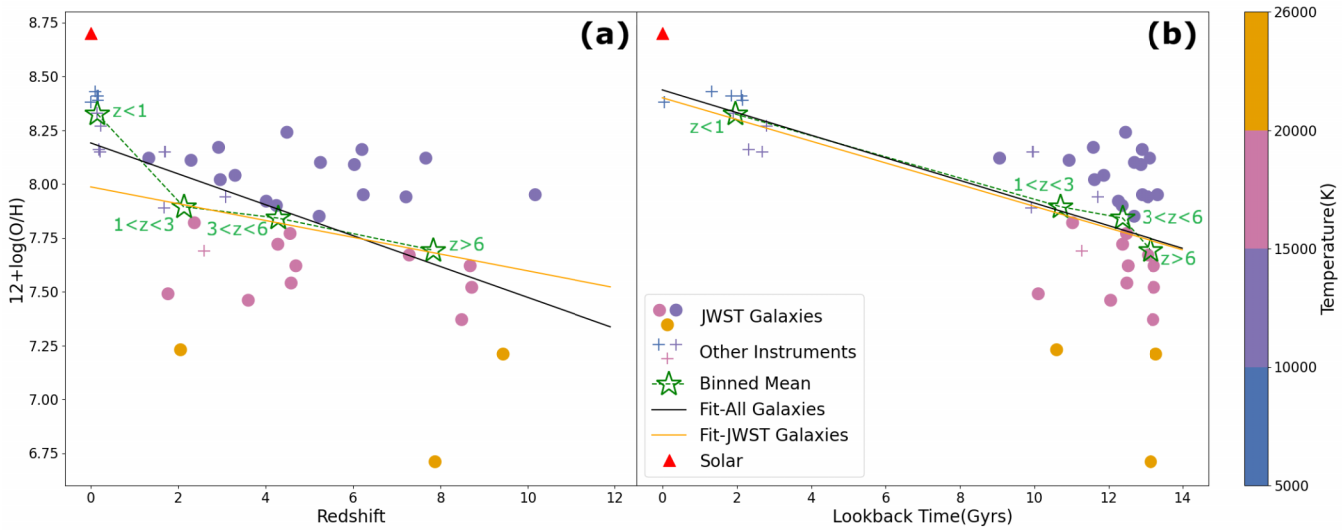

Figure 5. Oxygen abundance evolution with redshift (a) and lookback time (b) using J. E. Méndez-Delgado et al. (2023) formula.

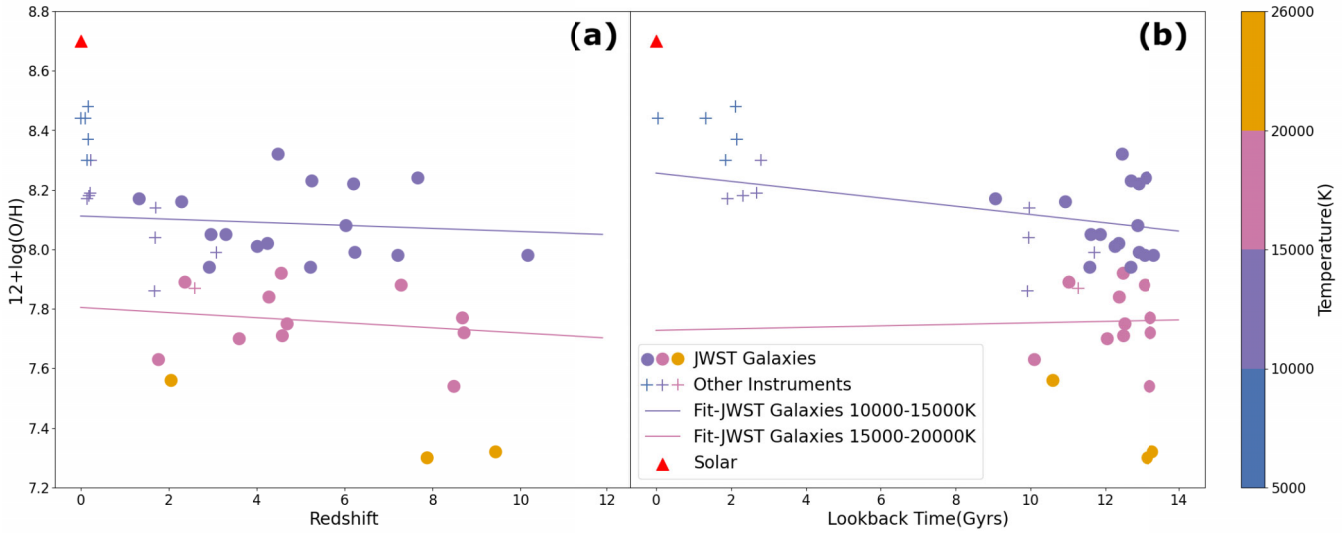

Figure 6. Oxygen abundance evolution with redshift (a) and lookback time (b) using Y. I. Izotov et al. (2006) formula, with fitting to 10 000–15 000 K and 15 000–20 000 K temperature bins separately.

4.4.1 *K-means clustering*

We determine the optimal cluster count using the elbow method, in which within-cluster sum of squares (WCSS) is computed for $k = 1$–10 and plotted against k. The elbow, defined as the point of maximum curvature where additional clusters yield diminishing reduction in WCSS, occurs at $k = 3$. Employing the elbow method, we identify $k = 3$ as the optimal cluster number. The three clusters exhibit distinct physical characteristics (Fig. 8):

(i) **Cluster 0** (Local/Intermediate, $n = 17$): $\langle z \rangle = 1.39 \pm 1.58$, $\langle T_e \rangle = 10{,}953 \pm 1{,}120$ K, $\langle 12 + \log(\mathrm{O/H}) \rangle = 8.29 \pm 0.15$
(ii) **Cluster 1** (Early Universe, $n = 10$): $\langle z \rangle = 6.18 \pm 2.65$, $\langle T_e \rangle = 17{,}960 \pm 1{,}336$ K, $\langle 12 + \log(\mathrm{O/H}) \rangle = 7.68 \pm 0.15$
(iii) **Cluster 2** (High-Redshift, $n = 18$): $\langle z \rangle = 4.73 \pm 2.26$, $\langle T_e \rangle = 14{,}439 \pm 1{,}989$ K, $\langle 12 + \log(\mathrm{O/H}) \rangle = 8.02 \pm 0.13$

Analysis of variance confirms these clusters are statistically distinct ($F = 57.43$, $p < 0.001$). One-way ANOVA across the three cluster groups yields $F = 57.43$ ($p < 0.001$), where F is the ratio of between-cluster variance to within-cluster variance for $12 + \log(\mathrm{O/H})$; values substantially above 1.0 indicate that cluster means differ beyond what random sampling would produce. The clustering naturally separates galaxies by cosmic epoch, with clear trends in both temperature and metallicity.

4.4.2 *Predictive regression models*

We evaluate four regression algorithms: Linear Regression, Ridge Regression ($\alpha = 1.0$), Random Forest, and Gradient Boosting, using z and T_e as predictors. Performance is assessed via 70–30 train-test split with fivefold cross-validation.

Ridge Regression achieves $R^2 = 0.832$ on the 30 per cent held-out test set ($n = 14$ galaxies), with Root Mean Square Error (RMSE) = 0.128 dex and Mean Absolute Error (MAE) = 0.089 dex (Table 1). However, fivefold cross-validation yields $R^2 = 0.34 \pm 0.86$, indicating substantial instability across folds attributable to the limited training sample ($n = 45$). The gap between test-set

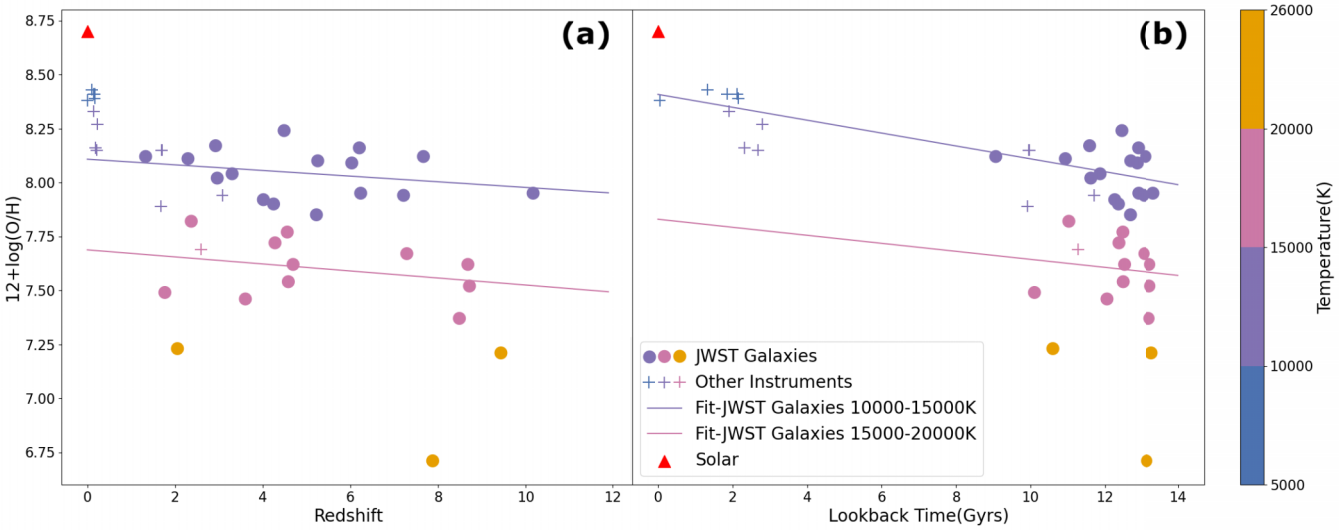

Figure 7. Oxygen abundance evolution with redshift (a) and lookback time (b) using J. E. Méndez-Delgado et al. (2023) formula, with fitting to 10 000–15 000 K and 15 000–20 000 K temperature bins separately.

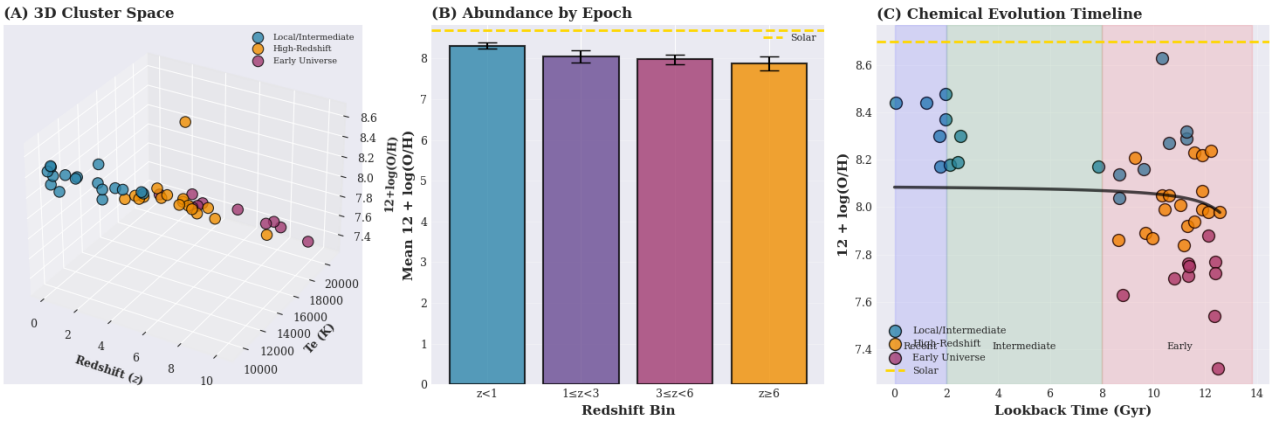

Figure 8. K-Means clustering results. *Left:* 3D parameter space showing three distinct clusters corresponding to cosmic epochs. *Center:* Mean oxygen abundance by redshift bin with 95 per cent confidence intervals, demonstrating systematic evolution. *Right:* Chemical evolution timeline with lookback time, showing approach to solar abundance (gold dashed line) at low redshift. Shaded regions indicate cosmic epochs: Recent (blue), Intermediate (green), and Early (red) Universe.

Table 1. Regression model performance metrics.

Model	R^2 (test)	RMSE (dex)	MAE (dex)	R^2 (CV)
Linear regression	0.832	0.128	0.089	0.34 ± 0.86
Ridge regression	**0.832**	**0.128**	**0.089**	0.34 ± 0.86
Random forest	0.642	0.186	0.110	0.18 ± 0.70
Gradient boosting	0.328	0.255	0.131	-0.55 ± 1.42

and cross-validated performance reflects that the held-out test partition may not represent the full parameter range. Given this limitation, the Ridge model should be interpreted as an interpolation tool for galaxies within the observed parameter range (T_e = 9100–25 500 K, $z = 0.003$–10.167) rather than a general predictive formula.

To illustrate practical use, we apply the trained Ridge model to CEERS-1019 ($z = 8.679$, $T_e = 17\,000$ K) using a leave-one-out procedure, withholding its measured abundance from the training set. The model predicts $12 + \log(\mathrm{O/H}) = 7.79$, compared to the directly derived value of 7.77 (Izotov method, Table A2), a residual of 0.017 dex, well within the 95 per cent prediction interval of ± 0.246 dex. This example illustrates how the model can provide a rapid abundance estimate for a galaxy where [O III] λ4363 is detected but a full T_e-based derivation is unavailable due to missing [O II] or [S II] lines.

The Ridge model predictions with 95 per cent bootstrap confidence intervals (1000 iterations) are shown in Fig. 9. Residual analysis reveals no systematic trends with redshift (slope: -0.003 ± 0.008), confirming the model captures the functional form adequately. The 95 per cent prediction interval of ± 0.246 dex is comparable to typical measurement uncertainties.

4.4.3 Redshift-binned evolution

We partition the sample into four redshift bins and calculate weighted means (Table 2). The systematic decrease of Δ[12 +

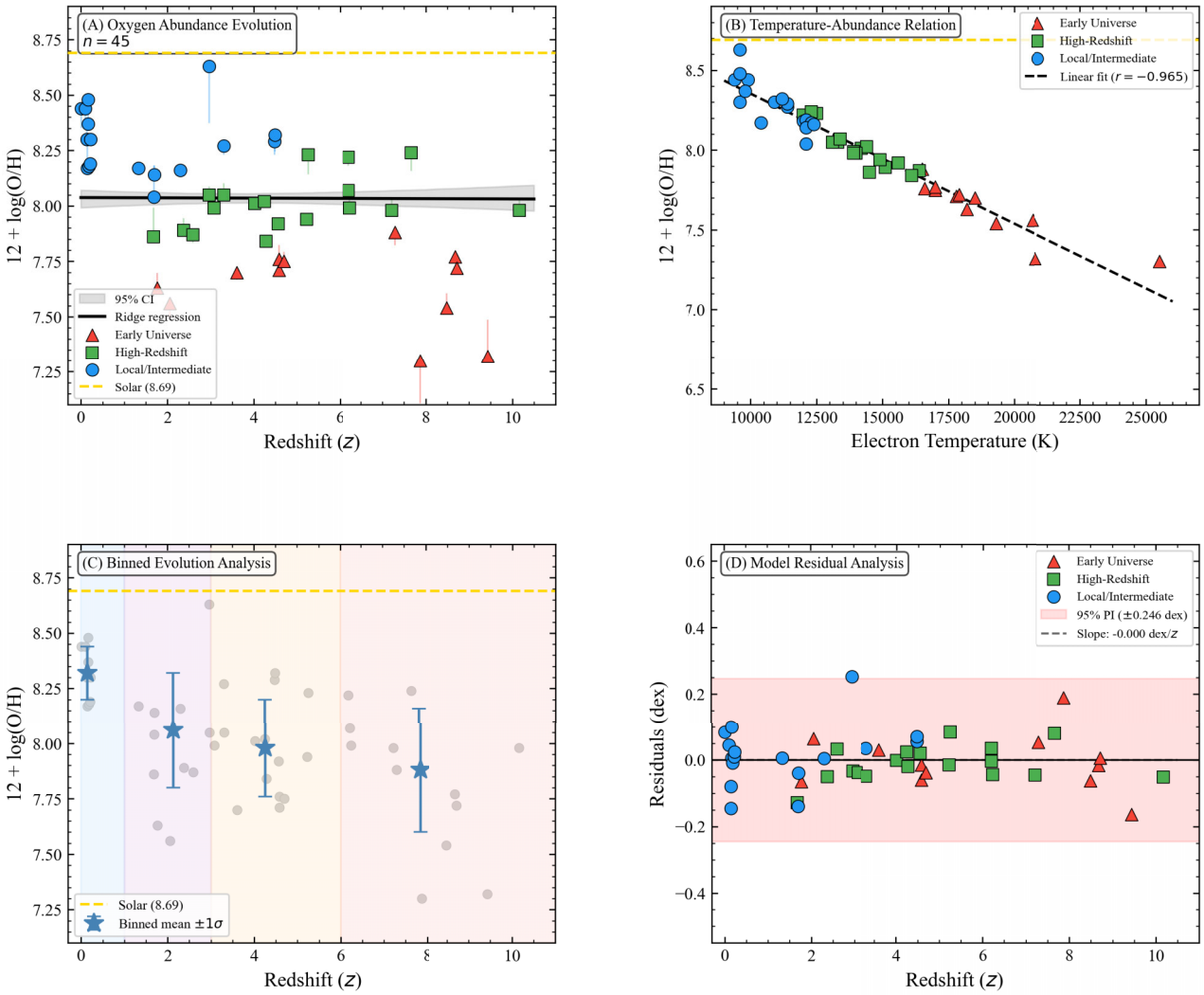

Figure 9. Machine learning regression analysis. (a) Oxygen abundance evolution with redshift, coloured by cluster membership. Ridge regression prediction (black line) with 95 per cent bootstrap confidence interval (grey shading). Solar abundance shown as gold dashed line. Vertical lines connect each galaxy to the Ridge regression prediction, illustrating individual deviations. The scatter about the trend is comparable to or exceeds typical measurement uncertainties, particularly at $z > 6$ where the standard deviation within the early Universe cluster (0.15 dex) matches the full prediction interval. (b) Temperature-abundance relation demonstrating strong anticorrelation ($r = -0.878$, $p < 0.001$). (c) Binned evolution with error bars showing systematic enrichment (individual galaxies in grey). (d) Model residual analysis showing no systematic trends and 95 per cent prediction interval (red shading, ±0.246 dex).

log(O/H)] = 0.44 dex from $z \sim 8$ to present corresponds to a factor of ∼2.8 increase in absolute oxygen abundance. Linear regression on binned means yields a slope of -0.052 ± 0.012 dex per unit z ($p < 0.001$), though the best-fit is better described by non-linear evolution approaching solar values asymptotically at $z \to 0$.

4.4.4 *Physical interpretation*

The superior performance of the bi-variate Ridge model demonstrates that chemical evolution cannot be captured by redshift alone. The strong temperature-abundance anticorrelation ($r = -0.878$, $p < 0.001$) explains much of the scatter in z-abundance space, reflecting diverse ionization conditions and star formation histories among galaxies at fixed epochs. The systematic enrichment from $z \sim 10$ to present is consistent with hierarchical galaxy formation where progressive stellar nucleosynthesis enriches the ISM over cosmic time.

Table 2. Redshift-binned oxygen abundance statistics.

Bin	n	$\langle z \rangle$	12+log(O/H)	$\langle T_e \rangle$ (K)
$z < 1$	9	0.15 ± 0.07	8.32 ± 0.12	$10{,}411 \pm 1{,}036$
$1 \leq z < 3$	11	2.13 ± 0.55	8.06 ± 0.26	$14{,}245 \pm 3{,}188$
$3 \leq z < 6$	14	4.25 ± 0.69	7.98 ± 0.22	$14{,}593 \pm 2{,}446$
$z \geq 6$	11	7.84 ± 1.36	7.88 ± 0.28	$15{,}545 \pm 2{,}929$

The $k = 3$ clustering solution, derived without prior knowledge of redshift labels, partitions galaxies into groups that correspond to the physically motivated redshift bins in Table 2: Cluster 0 (local/intermediate, $z = 0$–3) recovers the high-metallicity, low-temperature population; Cluster 1 (early universe, $z > 6$) recovers the low-metallicity, high-temperature systems identified in Section 4.3; and Cluster 2 (high-redshift, $3 < z < 6$) spans the intermediate regime. The correspondence between an unsupervised algorithm and physically motivated groupings confirms that the

T_e-O/H-redshift covariance structure in the data is not an artefact of the specific calibration formulas. The Ridge model predictive capability ($R^2 = 0.832$ on the test partition, RMSE = 0.128 dex) quantifies the degree to which T_e and z together constrain 12 + log(O/H), and provides a basis for rapid abundance estimation in future large *JWST* samples where direct T_e measurement is unavailable.

4.5 Metallicity evolution

It is useful to relate universal chemical evolution of oxygen abundance to metallicity versus z from *JWST* and other observatories. There is a correlation between stellar mass and metallicity, the mass–metallicity relation (MZR), as well as the dependence on star formation rate (SFR) leading to the so-called fundamental metallictiy relation (FMR). However, while the overall trend underlying MZR and FMR seems well-established (e.g. C. A. Tremonti et al. 2004; F. Mannucci et al. 2010), deviations therefrom are numerous. Precise delineation of gradients is unclear owing to factors such as the presence of AGN, supernova winds, stellar feedback and galactic outflows(M. Koller et al. 2026).

Metallicity determination and gradients entails abundances of α elements and Fe. For example, Arellano *et al.* 2022 find that C, N, and O abundance ratios at $z \sim 5$ are comparable to star-forming galaxies at $z \sim 0$ with $\log(M/M_\odot) \sim 8$ and $Z \sim 0.2 - 0.3 Z_\odot$. EXCELS surveys are measuring O, Ne, and Ar (e.g. K. Z. Arellano-Córdova et al. 2022b; T. M. Stanton et al. 2025). The Fe abundance is related to core-collapse Type II SNe via abundance ratios relative to Fe, and enrichment due to subsequent contributions from Type Ia SNe out to $z \sim 12$ (M. Nakane et al. 2025).

One useful pathway to gas phase metallicity is to analyse forbidden nebular [Fe II] lines in conjuction with [O III] lines as herein. There are several well-known [Fe II] O/NIR lines that we have studied extensively with theoretical computations of atomic data and emissivity ratios (A. K. Pradhan & H. L. Zhang 1993; M. A. Bautista et al. 1995; H. L. Zhang & A. K. Pradhan 1995). But observed Fe spectral data are sparse for high-z galaxies with few exceptions. Nevertheless, using earlier [Fe/H] values M. Nakane et al. (2025), and [O/H] derived in the present work, we may compare z-averaged [O/Fe] ratios. In Table 2, we have the redshifted-binned 12 + log(O/H) = 7.84±1.36 for all $< z > \geq 6$ galaxies in our sample, and consistent with an average value of [12 + log(O/H)] = 7.77 from Nakane et al. for 8 galaxies with z = 9-12, albeit with a large disperson ranging from 7.44 to 8.31. Their dispersion in [O/Fe] ranges from +1.92 to −0.72 with an average <[O/Fe]> = −0.33. Combining earlier iron values with our oxygen abundances we obtain <[O/Fe]> = −0.01 for high-z. However, since these value differ substantially for individual galaxies and deviations from MZR and FMR, it is difficult to ascertain overall chemical evolution on average, except to note that the oxygen abundance evolves marginally slower than the increase in iron abundance.

5 DISCUSSION

With the aim of ascertaining a systematic pattern in metallicity with oxygen abundance as a probe, we have analysed *JWST* spectra of galaxies spanning a range of redshifts from z = 0–10, with the following findings and several important caveats, constraints and conundrums of the present study:

1. Broadly speaking, the results presented in the previous section demonstrate a decreasing trend in O/H with redshift as shown in Figs 4 and 5. In each z-range selected for binning the large sample of galaxies the downward trend is discernible overall. The decreasing pattern holds according to the best linear fits as well as averages in each z-binned range.

2. Focusing on *JWST* galaxies in Figs 4 and 5, which representing oxygen evolution from z = 1.3293 to z = 10.167, the linear best-fitting between oxygen abundance and redshift gives a slope of −0.0276 and −0.0390, with y-intercept of 8.04 and 7.99, respectively. The slopes are relatively shallow, suggesting a slow evolution of metallicity in high-redshift galaxies. An earlier work A. Sarkar et al. 2024 employed a strong linear calibration method for data analysis mainly from JADES public Data Release 3 and *JWST*-PRIMAL Legacy Survey ranging from z = 4–10, also suggested a slow evolution with a slope of -0.067 ± 0.013, which differs from but is close to the slope in our work. That implies that our direct T_e-based method of [O III] line ratios analysis with independent atomic processes modelling basically agrees with the strong line results in the general evolution trend of oxygen abundance with z. The data sets of our work do not entirely overlap with A. Sarkar et al. 2024, and therefore this agreement lends more credibility to the overall trend. While a larger sample may still be useful, these two studies appear to confirm the slow evolution of oxygen as a metallicity probe up to the early universe.

3. Whereas the lowest O-abundance is found to be 6.75 relative to solar value 8.70, the overall fits exhibit a significantly larger abundance distribution ranging from 7.50 to 8.25. That is consistently less than solar but still quite considerable, implying rapid stellar nucleosynthesis in the early Universe well beyond a lookback time of 13 Gyr (Figs 4 and 5).

4. There is a marked difference in O-abundance relative to electron temperature. In fact, Fig. 4 exhibits a clear dichotomy between higher temperature *JWST* galaxies with $T_e > 15\,000K$ and significantly lower oxygen abundances (pink and yellow dots), compared to those with lower temperatures with $T_e < 15\,000K$ (purple dots). The scatter around the lines of best linear fit may be a measure of uncertainty in the determination of temperatures. Nonetheless, the bi-modal distribution in O-abundance with temperature seems manifest from the results derived, as shown explicitly in Fig. 6 and 7, with differential O-abundances up to ∼ 0.3 dex for the two distributions. The three galaxies with $T_e > 20\,000K$ (yellow dots) most clearly elicit the inverse correlation of low O-abundance with temperature down to 12 + log(O/H) = 6.75 (Fig. 6,7).

5. The spectral diagnostics is based on nebular lines of [O II], [O III], and [S II] used to determine temperatures and densities in H II regions. Assuming that the brightest H II regions observed from high-z galaxies are due to massive stars with the shortest stellar lifespan, the spectral analysis would sample the earliest stellar formation in host galaxies. As such, the O-abundances thereby determined should correspond to metals formed close to the epochs of the earliest Type II supernovae, that are the predominant sources of α-element nucleosynthesis.

6. Additional uncertainties in nebular spectral analysis may occur owing to temperature fluctuations and (e + ion) recombinations from higher ionization stages than O III. That is a topic that requires a much larger atomic model for O III than considered herein. We have ensured that the atomic data are consistent and accurate for the five-level EIE model as well as the extended CRR model. Two different EIE data sets have been employed (Storey and Sochi 2012 and Palay et al. 2012), and both yield results for [O III] line ratios in the temperature range of interest, 5000–20 000 K, that are in excellent agreement for a wide

range of nebular densities (Fig. 1). Combined with the O II and S II atomic data for density diagnostics they yield the coloured contour temperature-density plots shown in Fig. 2. The much larger CRR model than EIE employs accurate R-matrix data for level-specific (e + ion) RRCs from NORAD (Nahar 2020, 2024). Altogether, the atomic data lend confidence to the accuracy of computed line ratios. Therefore, the temperature-abundance dichotomy manifest in results shown as bi-modal distribution in Fig. 6. Whereas the effect of recombination on forbidden [O III] line ratios in the five-level system is negligible, the extended CRR model is likely to be considerable importance in ascertaining the effect on recombination lines of O III via the Bowen fluorescence mechanism (e.g. A. K. Pradhan & S. N. Nahar 2011.)

7. [O III] emitters at high- z may be host galaxies with AGN. An important caveat here is the role of AGN contributions. The line ratio analysis presented herein does not distinguish between broad line regions of AGN in nebular conditions, other H II regions ionized by massive stars and supernova remnants in nebular phase. As such, further work is needed to address interesting questions related to formation of supermassive black holes in the early universe, clustering of galaxies and quasars (Huang et al. 2026), and objects such as Little Red Dots that may be heavily obscured AGN with similar spectral signatures (Kokorev et al. 2025). The extended CRR model mentioned in item 6 could possibly distinguish between purely nebular [O III] line ratios, and those including recombination under different conditions where higher ionization species such as O IV may be present with significant ion fractions.

8. Results from ground-based data from Keck and VLT instruments up to $z \sim 3$ falls within the low-z values of up to 12 + log(O/H) = 8.5–7.9, and lie in between *JWST* observations of galaxies with similar redshifts. That underpins the derived trend of O-abundance with z at lower redshifts than those observed by *JWST*.

9. In addition to physical correlations in this work, there may also be others such as masses of galaxies that could be related to Type II SNe rates, as well as AGN in active or dormant phases. Whereas the role of massive stars in rapid nucleosynthesis of α elements is evident, it would also be of interest to carry out similar spectral studies of other elements such as nitrogen whose abundance proportion to oxygen might indicate possible contributions from slower nucleosynthesis in low-mass AGB stars.

10. Statistical Validation and Uncertainty Quantification: The machine learning component served a dual purpose: (1) providing rapid abundance estimates for future large samples where full photoionization modelling is computationally expensive, and (2) quantifying the predictive power of our physical parameter space. The K-means clustering naturally identified three cosmic epochs with statistically distinct properties ($F = 57.43$, $p < 0.001$). The 95 per cent prediction interval of ± 0.246 dex from the Ridge model is comparable to typical measurement uncertainties, suggesting we have captured the dominant physical trends.

11. We compare the overall metallicity by comparing the z-averaged <[O/Fe]> using the present determination of oxygen abundance and correlating with earlier determination of [Fe/H] and [O/Fe] for high-z galaxies, and find a weaker correlation for metallicity evolution. However, other factors that determine the MZR and FMR lead to large dispersions, not related to metallicity evolution per se, but by SFR, AGN feedback, delay time evolution of SNe 1a (D. H. Weinberg, B. H. Andrews & J. Freudenburg 2017).

6 CONCLUSIONS

The main conclusion of the meta-analysis presented in this paper is that there is a slow but distinct and systematic trend in the decrease of oxygen abundance with increasing redshift up to $z > 10$. The analysis depended on a re-examination of line ratios of [O III] lines, together with [O II] and [S II] calculated line emissivities and observed line intensity ratios. Despite the scatter in derived parameters from a fairly large sample of galaxies, the overall trend and redshift-averaged values appear to lead to the same conclusion. However, the results also demonstrate and confirm earlier observational works based on *JWST* data that metallicities in high-z galaxies were already significant before a lookback time of up to 13 Gyr and formation of H II regions by massive stars in the early Universe. While the oxygen abundance is smaller by up to one dex or more compared to galaxies in the present epoch, the deficiency is not larger. In that sense, stellar formation and mass–metallicity relations would appear to hold for high-z galaxies that are similar to evolved ones at low-z, as have been established in previous studies.

We have attempted to expand the analysis beyond what is inferred directly from observational data using a basic machine learning algorithm that validates these trends statistically. The Ridge regression analysis achieves $R^2 = 0.832$, confirming the strong T_e-abundance anticorrelation. The comprehensive data analytics workflow developed for this study integrates atomic physics calculations, empirical calibrations, and machine learning validation providing a reproducible framework applicable to the larger galaxy samples anticipated from upcoming *JWST* surveys, enabling systematic constraints on cosmic chemical evolution at scale.

We do not find a significant correlation between [O/Fe] versus z when averaged over the high-z galaxies in our sample. However, this result is uncertain owing to paucity of data for iron in our sample as well as previous studies, and owing to large dispersion among individual galaxies. While the oxygen abundance shows a distinct albeit slow evolution with z, more data are needed to ascertain metallicity evolution precisely. We expect to continue these studies with high$-z$ spectra of iron and other elements.

ACKNOWLEDGEMENTS

This work was partially supported by the U.S. National Science Foundation through grant AST-2407470. The R-matrix calculations were carried out at the Ohio Supercomputer Center and on OSU computer clusters. This work applied the following Python package: ASTROPY (Astropy Collaboration et al. 2013, ASTROPY Collaboration et al. 2018, and ASTROPY Collaboration et al. 2022), SCIPY (P. Virtanen et al. 2020), matplotlib(J. D. Hunter 2007), and NUMPY(C. R. Harris et al. 2020).

DATA AVAILABILITY

The data employed in our studies, including atomic data and line emissivities, are available from the authors and from S. Nahar 2020.

REFERENCES

Abdurro'uf et al., 2024, ApJ, 973, 47
Acharyya A. et al., 2019, MNRAS, 488, 5862
Arellano-Córdova K. Z. et al., 2022a, ApJ, 940, L23

Arellano-Córdova K. Z. et al., 2022b, ApJ, 940, L23
Arellano-Córdova K. Z. et al., 2025, MNRAS, 540, 2991
Astropy Collaboration, 2013, A&A, 558, A33
Astropy Collaboration, 2018, AJ, 156, 123
Astropy Collaboration, 2022, ApJ, 935, 167
Bautista M. A., Depoy D. L., Pradhan A. K., Elias J. H., Gregory B., Phillips M. M., Suntzeff N. B., 1995, AJ, 109, 729
Berg D. A. et al., 2022, ApJS, 261, 31
Bhattacharya S., Arnaboldi M., Gerhard O., Kobayashi C., Saha K., 2025, ApJ, 983, L30
Bunker A. J. et al., 2024, Astronomy & Astrophysics, 690, A288
Chen Y. et al., 2024, preprint (arXiv:2405.18476)
Clarke L. et al., 2023, ApJ, 957, 81
Curti M. et al., 2022, MNRAS, 518, 425
Curti M. et al., 2025, A&A, 697, A89
Decarli R. et al., 2024, A&A, 689, A219
Dopita M. A., Sutherland R. S., 2013, Astrophysics of the Diffuse Universe. Springer, Berlin, Heidelberg, Germany
Gburek T. et al., 2019, ApJ, 887, 168
Harikane Y. et al., 2025, ApJ, 993, 204
Harris C. R. et al., 2020, Nature, 585, 357
Hoy K., Nahar S. N., Pradhan A. K., 2023, Monthly Notices of the Royal Astronomical Society: Letters, 521, L48
Hsiao T. Y.-Y. et al., 2024, ApJ, 973, 81
Hsiao T. Y.-Y. et al., 2025, ApJ, 993, 70
Hunter J. D., 2007, Computing in Science and Engineering, 9, 90
Inkenhaag A. et al., 2025, MNRAS, 541, 3837
Isobe Y., Ouchi M., Nakajima K., Harikane Y., Ono Y., Xu Y., Zhang Y., Umeda H., 2023, ApJ, 956, 139
Izotov Y. I., Stasińska G., Meynet G., Guseva N. G., Thuan T. X., 2006, Astronomy & Astrophysics, 448, 955
Jain S. et al., 2025, ApJ, 1000, 109
Koller M. et al., 2026, Metal Mayhem at z ∼ 7 − 10: Diversity and Evolution of Gas-Phase Metallicity Gradients, preprint (arXiv:MNRAS 2026), https://arxiv.org/abs/2604.07076
Li S. et al., 2025, ApJ, 979, L13
Loaiza-Agudelo M., Overzier R. A., Heckman T. M., 2020, The Astrophysical Journal, 891, 19
Mannucci F., Cresci G., Maiolino R., Marconi A., Gnerucci A., 2010, MNRAS, 408, 2115
Mascia S. et al., 2024, A&A, 690, A2
Matsuoka Y. et al., 2025, ApJ, 988, 57
Méndez-Delgado J. E., Esteban C., García-Rojas J., Kreckel K., Peimbert M., 2023, Nature, 618, 249
Mingozzi M. et al., 2022, The Astrophysical Journal, 939, 110
Morishita T. et al., 2025, ApJ, 985, 83
Nahar S., 2020, Atoms, 8, 68
Nahar S. N., 1999, ApJS, 120, 131
Nakajima K., Ouchi M., Isobe Y., Harikane Y., Zhang Y., Ono Y., Umeda H., Oguri M., 2023, ApJS, 269, 33
Nakane M. et al., 2025, ApJ, 994, 65
Palay E., Nahar S. N., Pradhan A. K., Eissner W., 2012, MNRAS, 423, L35
Pradhan A. K., Nahar S. N., 2011, Atomic Astrophysics and Spectroscopy. Cambridge Univ. Press, Cambridge
Pradhan A. K., Zhang H. L., 1993, ApJ, 409, L77
Rogers N. S. J., Strom A. L., Rudie G. C., Trainor R. F., Raptis M., von Raesfeld C., 2024, ApJL, 964, L12
Sanders R. L. et al., 2016, ApJ, 825, L23
Sanders R. L., Shapley A. E., Topping M. W., Reddy N. A., Brammer G. B., 2023b, Direct Te-based Metallicities of z=2-9 Galaxies with JWST/NIRSpec: Empirical Metallicity Calibrations Applicable from Reionization to Cosmic Noon, preprint (arXiv:2303.08149), https://arxiv.org/abs/2303.08149
Sanders R. L., Shapley A. E., Topping M. W., Reddy N. A., Brammer G. B., 2023, ApJ, 962, 24
Sarkar A. et al., 2025, ApJ, 978, 136
Stanton T. M. et al., 2025, MNRAS, 537, 1735
Stiavelli M. et al., 2024, ApJ, 981, 136
Storey P. J., Sochi T., 2015, MNRAS, 449, 2974
Tremonti C. A. et al., 2004, The Astrophysical Journal, 613, 898
Virtanen P. et al., 2020, Nature Methods, 17, 261
Weinberg D. H., Andrews B. H., Freudenburg J., 2017, ApJ, 837, 183
Welch B. et al., 2024, ApJ, 975, 196
Welch B. et al., 2025, ApJ, 980, 33
Witstok J. et al., 2024, MNRAS, 536, 27
Zhang H. L., Pradhan A. K., 1995, A&A, 293, 953
Zhang Y., Morishita T., Stiavelli M., 2026, ApJ, 998, 141
Zhu C. et al., 2025, ApJ, 982, 27

APPENDIX A: DATA COLLECTION OF ANALYSIS RESULTS AND LINE FLUXES FROM LITERATURE

Table A1. A holistic table of line fluxes from other papers.

Galaxy	z	O II3726	O II3729	O III4363	O III4959	O III5007	S II6718	S II6732	O II7320	O II7330	Hβflux (erg s^{-1} cm^{-2})
Haro3	0.003208	1.243	1.577	0.02521	1.361	4.016	0.1461	0.1172	–	–	–
J0021+0052	0.09839	0.6407	0.7217	0.02202	1.537[c]	4.427	0.1819	0.1312	0.02554	0.01982	$2.271 \cdot 10^{-14}$
J032845.99+011150.8	0.142181	2.154[a]	–	0.01280	0.7333	2.294	0.2849	0.2191	0.02312	0.01920	$2.812 \cdot 10^{-15}$
J015028.39+130858.4	0.146712	2.220[a]	–	0.01650	0.7424	2.221	0.2570	0.2205	0.01881	0.01568	$6.059 \cdot 10^{-15}$
J124509.05+104340.1	0.165569	1.775[a]	–	0.02845	1.718	5.122	0.1714	0.1435	0.02856	0.02243	$8.648 \cdot 10^{-15}$
J005527.45–002148.7	0.167449	2.008[a]	–	0.02228	1.236	3.673	0.1768	0.1573	0.03513	0.02718	$1.611 \cdot 10^{-14}$
J101629.88+073404.9	0.18271	2.271[a]	–	0.05832	1.729	5.236	0.1475	0.1231	0.02264	0.01852	$7.288 \cdot 10^{-15}$
J082247.66+224144.0	0.216226	2.090[a]	–	0.06771	1.924	5.814	0.1329	0.1225	0.03747	0.02757	$8.994 \cdot 10^{-15}$
J084034.10+134451.3	0.226961	1.785[a]	–	0.04537	1.784	5.353	0.1842	0.1465	0.02768	0.02191	$2.601 \cdot 10^{-15}$
GOODS-N-14595	1.67596	0.5759	0.6161	0.08929	1.692	4.960	0.2500	<0.5446	–	–	$2.240 \cdot 10^{-17}$
GOODS-N-8240	1.6909	0.5944	0.6285	0.04954	1.458	4.434	<0.9659	<5.399	–	–	$3.230 \cdot 10^{-17}$
RCSGA032727-132609	1.7	1.133	0.9876	0.05637	1.543	4.900	0.1448	0.1066	–	–	$4.495 \cdot 10^{-15}$
SGAS1723+34	1.3293	–	–	0.07480	2.084	6.239	0.1447	0.1076	0.02103	0.01935	$1.845 \cdot 10^{-15}$
NIRSpec3753	1.768	2.692[a]	–	0.1169	1.270	4.040	0.2770	0.2361	–	–	$8.810 \cdot 10^{-18}$
CEERS-3506	2.055	–	–	0.2350	2.530	6.510	0.01360	0.02230	0.007100	0.004200	$2.210 \cdot 10^{-17}$
CEERS-3788	2.295	0.4170	0.4590	0.08800	2.370	7.010	0.3720	0.2330	–	–	–
Sunburst Arc	2.37	0.2900	0.2200	0.1380	2.200	6.800	0.03900	0.04300	0.03000	0.02200	$6.600 \cdot 10^{-19}$
A1689-217	2.5918	1.156	1.339	0.1094	2.156	6.210[c]	–	–	–	–	$1.920 \cdot 10^{-16}$
SGAS1226+21	2.925	–	–	<0.04707	1.320	4.327	0.3045	0.2917	<0.006973	<0.006973	$1.721 \cdot 10^{-16}$
Q2343-D40	2.963	–	–	0.08700	1.993	5.914	0.1310	0.09700	0.02500	0.02000	$8.650 \cdot 10^{-18}$
Q2343-D40	2.963	–	–	0.04000	2.254	7.075	0.1310	0.09700	0.02500	0.02000	–
COSMOS-1908	3.08	0.2309	0.2309	0.1186	2.288	7.055	–	–	–	–	$4.720 \cdot 10^{-17}$
CEERS-11088	3.302	1.681[a]	–	0.05737	2.041	6.052	0.2147	0.1714	0.07257[b]	–	$2.632 \cdot 10^{-17}$
CEERS-11088	3.302	0.5200	0.4700	0.08800	1.936	6.233	0.5830	0.2570	–	–	–
JADES-19519	3.604	0.3790	0.5330	0.2010	2.279	6.782	–	–	–	–	–
GLASS-160133	4.015	0.2140	0.2610	0.1540	2.559	7.725	–	–	–	–	–
GTO1199-150880	4.247	1.006[a]	–	0.1358	10.26[d]	–	0.08447	0.06849	–	–	$8.760 \cdot 10^{-18}$
GRB050505	4.28	0.7037	0.9722	0.1389	2.065	6.046	0.2778	0.2037	–	–	$1.080 \cdot 10^{-17}$
CEERS-1665	4.482	1.514[a]	–	0.06532	2.214	6.827	0.1512	0.1243	< 0.08772[b]	–	$2.679 \cdot 10^{-17}$
CEERS-1665	4.488	0.5120	0.3520	0.06700	2.338	7.336	0.3100	0.2030	–	–	–
CEERS-1746	4.56	1.120[a]	–	0.1624	2.251	7.604	0.09117	0.09687	< 0.1425[b]	–	$3.510 \cdot 10^{-18}$
GLASS-150029	4.584	0.1780	0.2070	0.1840	2.328	6.588	–	–	–	–	–
GLASS-150029	4.584	0.1827	0.2373	0.1530	2.221	6.316	–	–	–	–	–
ID60001	4.6928	0.5650[a]	–	0.1640	2.170	6.470	0.04374	0.03645	–	–	$8.230 \cdot 10^{-18}$
EXCELS-121806	5.225	0.8411[a]	–	0.1339	2.327	6.826	0.05920	0.04835	–	–	$4.054 \cdot 10^{-18}$
EXCELS-70864	5.255	0.8541[a]	–	0.1108	2.854	8.617	<0.03900	<0.04446	–	–	$2.564 \cdot 10^{-18}$
J1211-0118	6.031	0.9760	1.163	<0.06200	1.605	4.783	–	–	–	–	$1.260 \cdot 10^{-17}$
J0217-0208	6.204	0.8930	0.6030	0.07500	2.004	6.567	–	–	–	–	$1.880 \cdot 10^{-17}$
J0217-0208	6.204	0.8930	0.6030	0.09592	2.234[c]	6.433	0.08931	0.09482	–	–	$9.070 \cdot 10^{-18}$
PJ308-21	6.2342	0.5/1.0/2.0[a,c]	–	0.1139	2.293	6.873	0.1418	0.1721	–	–	$1.650 \cdot 10^{-17}$
SXDF-NB1006-2	7.212	0.2660	0.2390	0.1130	2.262	6.741	–	–	–	–	$8.550 \cdot 10^{-18}$
GLASS-10021	7.286	0.3378	0.4730	0.1980	2.696	8.284	–	–	–	–	$7.400 \cdot 10^{-18}$
ERO6355	7.6651	0.5104	0.3896	0.1000	2.660	8.290	–	–	–	–	$2.110 \cdot 10^{-18}$
ZD12	7.8762	0.3300	0.2791	0.2529	7.051[d]	–	–	–	–	–	$6.090 \cdot 10^{-19}$
JADES-GS-z8-0-LA	8.48523	0.1402	0.08785	0.1776	1.836	5.470	–	–	–	–	$3.210 \cdot 10^{-19}$
CEERS-1019	8.6791	0.2084	0.1781	0.1780	2.262	7.011	–	–	–	–	$1.017 \cdot 10^{-17}$
JADES-GS-z8-1-LA	8.71523	0.2667	0.2309	0.2010	2.401	7.153	–	–	–	–	$8.360 \cdot 10^{-19}$
JADES-GS-z9-0	9.4327	0.07825	0.07294	0.1790	1.756	4.955	–	–	–	–	$7.540 \cdot 10^{-19}$
MACS0647-JD1	10.167	0.1038	0.07022	0.1130	2.396[c]	6.900	–	–	–	–	$3.275 \cdot 10^{-18}$

Note. All line fluxes are normalized by H$\beta = 1$.
[a]This is the blended flux for O II3726+O II3729.
[b]This is the blended flux for O II7320+O II7330.
[c]This is not come from papers, it is come from assumptions as shown in the text of Appendix A.
[d]This is the blended flux for O III4959+O III5007.

Table A2. Line flux data sources of galaxies.

Source	Instrument	Adopted line flux data of galaxies
A. Acharyya et al. (2019)	Keck/NIRSPEC	All data of RCSGA032727-132609.
Y. Chen et al. (2024)	Keck/KCWI	All data of Haro3.
L. Clarke et al. (2023)	Keck/MOSFIRE	All data of GOODS-N−14595 and GOODS-N−8240.
M. Loaiza-Agudelo, R. A. Overzier & T. M. Heckman (2020)	VLT/XShooter	All data of J032845.99+011150.8, J015028.39+130858.4, J124509.05+104340.1, J005527.45–002148.7, J101629.88+073404.9, J082247.66+224144.0,and J084034.10+134451.3.
M. Mingozzi et al. (2022)	CLASSY	All data of J0021+0052.
R. L. Sanders et al. (2016)	MOSDEF	All data of COSMOS-1908.
K. Z. Arellano-Córdova et al. (2025)	*JWST*/NIRSpec	All data of EXCELS-121806 and EXCELS-70864.
S. Bhattacharya et al. (2025)	*JWST*/NIRSpec	All data of CEERS-3788, the second row of CEERS-11088, the first row of GLASS-150029, JADES-19519, and the second row of CEERS-1665. OIII4363, OIII4960, and OIII5008 line fluxes of the second row of Q2343-D40.
R. Decarli et al. (2024)	*JWST*/NIRSpec	All data of PJ308-21.
Y. Harikane et al. (2025)	*JWST*/NIRSpec	All data of J1211-0118, SXDF-NB1006−2, and first row of J0217-0208. Line fluxes of OII 3726 and 3729 lines of the second row of J0217-0208
R. L. Sanders et al. (2023b)	*JWST*/NIRSpec	Blended line flux of OII 3726 and 3729 lines and all other line flux data of CEERS-1019. All data of CEERS-1746, the first row of CEERS-11088, and the first row of CEERS-1665.
Y. Isobe et al. (2023)	*JWST*/NIRSpec	OII 3726 and 3729 lines ratio of CEER-1019, ERO6355, GLASS-160133, and the second row of GLASS-150029.
M. Curti et al. (2022)	*JWST*/NIRSpec	Blended flux of OII 3726 and 3729 lines and all other line flux data of ERO6355.
T. Y.-Y. Hsiao et al. (2025)	*JWST*/NIRSpec	Line flux O III 5007($=226 \cdot 10^{-19}\ erg\,s^{-1}\ cm^{-2}$) of MACS0647-JD1.
T. Y.-Y. Hsiao et al. (2024)	*JWST*/NIRSpec	O III5007/Hbeta(=6.9) ratio of MACS0647-JD1.
Abdurro'uf et al. (2024)	*JWST*/NIRSpec	O II3726, O II3729, and O III4363 line fluxes of MACS0647-JD1.
B. Welch et al. (2024)	*JWST*/NIRSpec	All data of SGAS1226+21 and SGAS1723+34.
B. Welch et al. (2025)	*JWST*/NIRSpec	All data of Sunburst Arc.
Y. Matsuoka et al. (2025)	*JWST*/NIRSpec	All data except for fluxes of O II 3726 and 3729 lines of the second row of J0217-0208.
N. S. J. Rogers et al. (2024)	*JWST*/NIRSpec	All data of the first row of Q2343-D40. SII6718, SII6732, OII7320, and OII7330 line fluxes of the second row of Q2343-D40.
K. Nakajima et al. (2023)	*JWST*/NIRSpec	Blended line flux of OII 3726 and 3729 lines and all other line flux data of the second row of GLASS-150029, GLASS-10021, and GLASS-160133.
M. Curti et al. (2025)	*JWST*/NIRSpec	All data of JADES-GS-z9-0.
J. Witstok et al. (2024)	*JWST*/NIRSpec	All data of JADES-GS-z8-1-LA and JADES-GS-z8-0-LA.
C. Zhu et al. (2025)	*JWST*/NIRSpec	All data of CEERS-3506
T. Gburek et al. (2019)	Keck/MOSFIRE	All data of A1689-217.
A. J. Bunker et al. (2024)	*JWST*/NIRSpec	All data of NIRSpec3753.
A. Inkenhaag et al. (2025)	*JWST*/NIRSpec	All data of GRB050505.
S. Li et al. (2025)	*JWST*/NIRSpec	OII 3726 and 3729 lines ratio of GLASS-10021.
T. Morishita et al. (2025)	*JWST*/NIRSpec	All data of ZD12.
M. Stiavelli et al. (2024)	*JWST*/NIRSpec	All data of GTO1199-150880.
Y. Zhang, T. Morishita & M. Stiavelli (2025)	*JWST*/NIRSpec	All data of ID60001.

Table A3. A holistic table of analysis results by using P. J. Storey & T. Sochi (2015) EIE data.

Galaxy	Instrument	z	$12+\log(O/H)$ Izotov formula	$12+\log(O/H)$ MD formula[c]	$12+\log(O/H)$ Original papar[d]	T_e[O III] (K)	N_e[O II] (cm^{-3})	N_e[S II] (cm^{-3})
Haro3	Keck/KCWI	0.003208	8.44	8.38	8.309	9900	145	183
J0021+0052	CLASSY	0.09839	8.44	8.43	8.17[e]	9400	275	50
J032845.99+011150.8	VLT/XShooter	0.142181	8.30	8.41	8.30	9600	–	126
J015028.39+130858.4	VLT/XShooter	0.146712	8.17	8.33	8.30	10400	–	283
J124509.05+104340.1	VLT/XShooter	0.165569	8.48	8.41	8.54	9600	–	245
J005527.45–002148.7	VLT/XShooter	0.167449	8.37	8.39	8.47	9800	–	343
J101629.88+073404.9	VLT/XShooter	0.18271	8.18	8.16	8.33	12000	–	239
J082247.66+224144.0	VLT/XShooter	0.216226	8.19	8.15	8.39	12100	–	412
J084034.10+134451.3	VLT/XShooter	0.226961	8.30	8.27	8.37	10900	–	170
SGAS1723+34	JWST/NIRSpec	1.3293	8.17	8.12	8.13	12300	–	80
GOODS-N−14595	Keck/MOSFIRE	1.67596	7.86	7.89	>7.62	14500	391	–
GOODS-N−8240	Keck/MOSFIRE	1.6909	8.04	8.15	8.02	12100	377	–
RCSGA032727-132609	Keck/NIRSPEC	1.7	8.14/8.13[a]	8.15	8.19	12100	726	68
NIRSpec3753	*JWST*/NIRSpec	1.768	7.63	7.49	–	18200	–	275
CEERS-3506	*JWST*/NIRSpec	2.055	7.56	7.23	7.52	20700	–	3755
CEERS-3788	*JWST*/NIRSpec	2.295	8.16	8.11	7.91	12400	320	–
Sunburst Arc	*JWST*/NIRSpec	2.37	7.89	7.82	7.97	15100	1196	870
A1689-217	Keck/MOSFIRE	2.5918	7.87	7.69	8.06	16400	284	–
SGAS1226+21	*JWST*/NIRSpec	2.925	>7.94	>8.17	>8.04	<11900	–	489
Q2343-D40	*JWST*/NIRSpec	2.963	8.05	8.02	8.07	13300	–	73
Q2343-D40	*JWST*/NIRSpec	2.963	8.63	8.41	8.01[f]	9600	–	80
COSMOS-1908	MOSDEF	3.08	7.99	7.94	8.00	14000	491	–
CEERS-11088	*JWST*/NIRSpec	3.302	8.27	8.22	8.33	11400	–	175
CEERS-11088	*JWST*/NIRSpec	3.302	8.05	8.04	7.87[f]	13100	668	–
JADES-19519	*JWST*/NIRSpec	3.604	7.70	7.46	7.48	18500	58	–
GLASS-160133	*JWST*/NIRSpec	4.015	8.01	7.92	7.95[g]	14200	204	–
GTO1199-150880	*JWST*/NIRSpec	4.247	8.02	7.90	8.00	14400	–	195
GRB050505	*JWST*/NIRSpec	4.28	7.84	7.72	7.80	16100	73	53
CEERS-1665	*JWST*/NIRSpec	4.482	8.29	8.22	8.27	11400	–	217
CEERS-1665	*JWST*/NIRSpec	4.488	8.32	8.24	8.13	11200	1405	–
CEERS-1746	*JWST*/NIRSpec	4.56	7.92	7.77	7.95	15600	–	766
GLASS-150029	*JWST*/NIRSpec	4.584	7.71	7.54	7.53	17800	294	–
GLASS-150029	*JWST*/NIRSpec	4.584	7.76	7.66	7.70[g]	16600	143	–
ID60001	*JWST*/NIRSpec	4.6928	7.75	7.62	7.75	17000	–	236
EXCELS-121806	*JWST*/NIRSpec	5.225	7.94	7.85	7.97	14900	–	205
EXCELS-70864	*JWST*/NIRSpec	5.255	8.23	8.10	8.21	12500	–	∼ 961[k]
J1211-0118	*JWST*/NIRSpec	6.031	>8.08	>8.09	8.51	<12600	226	–
J0217-0208	*JWST*/NIRSpec	6.204	8.22	8.16	8.20	12000	1526	–
J0217-0208	*JWST*/NIRSpec	6.204	8.07	8.01	–	13400	–	743
PJ308-21	*JWST*/NIRSpec	6.2342	7.99/8.02/8.07[b]	7.95	–	13900	–	1206
SXDF-NB1006−2	*JWST*/NIRSpec	7.212	7.98	7.94	7.99	14000	701	–
GLASS-10021	*JWST*/NIRSpec	7.286	7.88	7.67	7.87[g]	16500	61	–
ERO6355	*JWST*/NIRSpec	7.6651	8.24	8.12	8.24[h]	12300	1074	–
ZD12	*JWST*/NIRSpec	7.8762	7.30	6.71	7.34	25500	1007	–
JADES-GS-z8-0-LA	*JWST*/NIRSpec	8.48523	7.54	7.37	7.481	19300	2329	–
CEERS-1019	*JWST*/NIRSpec	8.6791	7.77	7.62	7.78[i]	17000	893	–
JADES-GS-z8-1-LA	*JWST*/NIRSpec	8.71523	7.72	7.52	7.699	17900	885	–
JADES-GS-z9-0	*JWST*/NIRSpec	9.4327	7.32	7.21	7.41	20800	743	–
MACS0647-JD1	*JWST*/NIRSpec	10.167	7.98	7.95	7.79[j]	13900	1613	–

[a]Left value is calculated by using N_e[O II], and the right is by using N_e[S II]. Other galaxies with using both O II and S II electron density give same electron temperature and oxygen abundance, so they are just listed as one electron temperature and oxygen abundance value.
[b]From 3 assumptions of OII3726+O II3729 flux 0.5/1.0/2.0, respectively.
[c]Méndez-Delgado Formula. The uncertainty of $12+\log(O/H)$ derived by this formula for all galaxies is about 0.2.
[d]The oxygen abundances listed here are adopted from the original papers from which the line ratio data were obtained, as summarized in Table A2. When line ratios are compiled from multiple sources, we include citations alongside each oxygen abundance value to clearly indicate its origin.
[e]D. A. Berg et al. (2022).
[f]S. Bhattacharya et al. (2025).
[g]K. Nakajima et al. (2023).
[h]M. Curti et al. 2022).
[i]R. L. Sanders et al. 2023b).
[j](T. Y.-Y. Hsiao et al. 2024).
[k]Upper limit of both SII lines are used to get the line ratio, so it is a uncertain value.

This paper has been typeset from a TEX/LATEX file prepared by the author.